

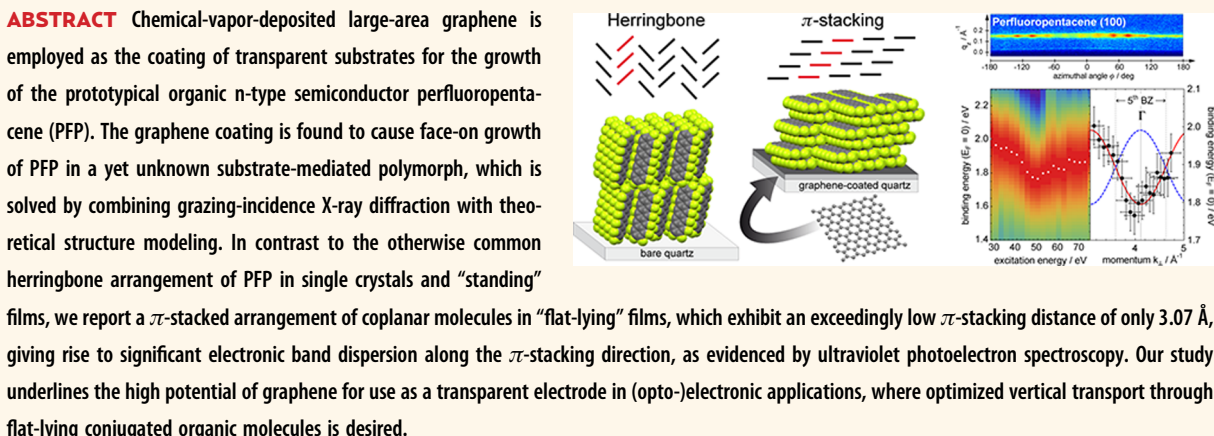
# Epitaxial Growth of $\pi$ -Stacked Perfluoropentacene on Graphene-Coated Quartz

Ingo Salzmann,<sup>†,\*</sup> Armin Moser,<sup>‡</sup> Martin Oehzelt,<sup>†,§</sup> Tobias Breuer,<sup>†</sup> Xinliang Feng,<sup>||</sup> Zhen-Yu Juang,<sup>||</sup> Dmitrii Nabok,<sup>¶,▼</sup> Raffaele G. Della Valle,<sup>#</sup> Steffen Duham,<sup>△</sup> Georg Heimel,<sup>†</sup> Aldo Brillante,<sup>#</sup> Elisabetta Venuti,<sup>#</sup> Ivano Bilotti,<sup>#</sup> Christos Christodoulou,<sup>†</sup> Johannes Frisch,<sup>†</sup> Peter Puschnig,<sup>¶,▲</sup> Claudia Draxl,<sup>¶,▼</sup> Gregor Witte,<sup>†</sup> Klaus Müllen,<sup>||</sup> and Norbert Koch<sup>†,§</sup>

<sup>†</sup>Institut für Physik, Humboldt-Universität zu Berlin, Berlin, Germany, <sup>‡</sup>Institute of Solid State Physics, Graz University of Technology, Graz, Austria,

<sup>§</sup>Helmholtz Zentrum Berlin für Materialien und Energie, BESSY II, Berlin, Germany, <sup>△</sup>Fachbereich Physik, Molekulare Festkörperphysik, Philipps-Universität Marburg, Marburg, Germany, <sup>||</sup>Max Planck Institute for Polymer Research, Mainz, Germany, <sup>#</sup>Department Materials Physics, University of Leoben, Leoben, Austria,

<sup>¶</sup>Dipartimento di Chimica Fisica e Inorganica and INSTM-UdR, Università di Bologna, Bologna, Italy, and <sup>▲</sup>Institute of Functional Nano & Soft Materials (FUNSOM), Soochow University, Suzhou, China



**KEYWORDS:** graphene · organic electronics · structure solution · pentacene · perfluoropentacene · band dispersion · grazing-incidence X-ray diffraction

Graphene, the two-dimensional hexagonal arrangement of  $sp^2$ -hybridized carbon, attracted unprecedented global research interest during the past decade.<sup>1–4</sup> This is due to its outstanding mechanical<sup>1–3</sup> and electronic<sup>4</sup> properties, which may be exploited in a broad range of applications, including field-effect transistors,<sup>5</sup> gas sensors,<sup>6</sup> optical modulators,<sup>7</sup> or organic electronics.<sup>8,9</sup> In particular, its high optical transparency together with its large charge-carrier mobility and low sheet resistance<sup>10–12</sup> renders graphene an ideal electrode material for (opto-)electronic applications<sup>9</sup> with the potential to replace high-cost tin-doped indium oxide (ITO) as standard transparent cathode.<sup>12,13</sup>

For organic electronics, in particular, one key charge-transport parameter is the transfer integral  $t$  expressing the ease of charge

transfer between adjacent molecules, which depends on intermolecular distance and mutual orientation.<sup>14–16</sup> As molecular organic semiconductors (OSCs) are generally anisotropic—exhibiting a layered bulk crystal structure with a typical edge-to-face herringbone (HB) arrangement<sup>17,18</sup> of molecules within one layer—also  $t$  and the charge transport are highly anisotropic;<sup>19</sup> the mobilities are generally higher within the HB layers. In order to increase  $t$  in that direction, considerable research efforts have been put toward modifying the molecular packing of OSCs from HB to a parallel arrangement of the molecular planes, referred to as  $\pi$ -stacking.<sup>20</sup> Indeed, such stacking can be favored over HB by the attachment of functional side groups,<sup>20</sup> as shown for bis(triisopropylsilyl)pentacene

\* Address correspondence to [ingo.salzmann@physik.hu-berlin.de](mailto:ingo.salzmann@physik.hu-berlin.de).

Received for review September 15, 2012 and accepted November 15, 2012.

Published online November 15, 2012  
10.1021/nn3042607

(TIPS-PEN).<sup>21,22</sup> Furthermore, it was recently demonstrated that, in such  $\pi$ -stacked films, reducing the intermolecular stacking distance from 3.33 to 3.08 Å and, hence, increasing  $t$ , increases hole mobilities in transistors from 0.8 to 4.6 cm<sup>2</sup> V<sup>-1</sup> s<sup>-1</sup>.<sup>23</sup> However, on common substrates like oxides (e.g., ITO), the  $\pi$ -stacking direction lies parallel to the substrate plane,<sup>23,24</sup> while out-of plane  $\pi$ -stacking is actually desired for (opto-)electronic applications, where current flows through the device vertically.

In contrast to ITO, typical OSCs adopt a face-on orientation on residue-free graphene, as evidenced in several studies for the monolayer regime.<sup>25–29</sup> In thicker films, however, where the intermolecular interaction predominates over the molecule–substrate interaction, a transition to the OSC bulk crystal structure, that is, the typical HB arrangement, is generally observed,<sup>29–31</sup> thereby limiting the vertical charge-carrier mobility, which is detrimental for (opto-)electronic applications, such as *vertical* organic field-effect transistors (v-OFETs).<sup>32–34</sup> In standard OFETs, the channel typically lies parallel to the dielectric substrate and, therefore, within the high-mobility directions of prototypical p- and n-type transistor materials like pentacene (PEN)<sup>35</sup> or perfluoropentacene (PFP),<sup>36</sup> respectively, which adopt a standing molecular orientation in such devices. For v-OFET, in contrast, enhanced vertical transport through both a molecular arrangement parallel to the substrate and optimized intermolecular orientation is sought.

In this study, we report on vertically  $\pi$ -stacked growth of PFP in films of application-relevant thickness with an exceedingly small  $\pi$ -stacking distance, which is induced by coating quartz substrates with graphene. This packing motif is in contrast to all reports so far, where a HB arrangement of PFP with an edge-to-face herringbone angle of almost 90° both in the single-crystal polymorph<sup>36</sup> and in a thin-film phase (TFP)—present on oxide substrates—prevails.<sup>37,38</sup> We carried out a full structure solution of this  $\pi$ -stacked polymorph (PSP) on graphene (and of the TFP on SiO<sub>x</sub>; see Supporting Information) by combining X-ray diffraction (XRD) methods with theoretical structure modeling. We provide evidence for the long-range epitaxial growth of this polymorph on graphene, that is, orientational registry of the molecules in the film with the underlying graphene layer. Furthermore, all of our experiments are corroborated by measurements on highly oriented pyrolytic graphite (HOPG) as reference, where an identical growth is evidenced by complementary experimental techniques. Finally, by employing ultraviolet photoelectron spectroscopy (UPS), we report electronic band dispersion of the highest occupied molecular orbital (HOMO) derived band in the  $\pi$ -stacking direction, which allows determining the value of the transfer integral  $t$  and, finally, estimating the hole mobility  $\mu_h$ .<sup>39</sup>

## RESULTS AND DISCUSSION

Graphene used throughout this work was synthesized through chemical vapor deposition (CVD) of methane on copper foil at 1020 °C substrate temperature with an ensuing wet transfer procedure to supporting quartz glass.<sup>41</sup> A representative Raman spectrum of the sample is depicted in Figure 1a, which shows a symmetric 2D band at 2686 cm<sup>-1</sup> with an intensity ratio to the G peak of 3.4:1. It can be fitted by a single Lorentzian (full width at half-maximum = 39 cm<sup>-1</sup>), thus evidencing the sample to be predominantly single-layer graphene. The D band contribution at 1355 cm<sup>-1</sup> is related to crystal size effects<sup>42</sup> due to defects and grain boundaries from the CVD growth process.<sup>43,44</sup> This graphene-coated quartz sample served as the substrate for a vacuum-deposited PFP film with 30 nm nominal film thickness, as measured by a quartz crystal microbalance.

Figure 1b shows a specular XRD scan of the film compared to that of a PFP/HOPG reference. (For an explicit comparison between specular X-ray diffraction on graphene-coated and noncoated quartz, see the Supporting Information.) Both films show a strong diffraction feature at  $q_z = 2.06 \text{ \AA}^{-1}$ , which cannot be explained by either of the two known HB polymorphs of PFP, that is, the single-crystal polymorph<sup>36</sup> as well as the TFP (see Supporting Information), evidencing the presence of the yet unknown PSP. Note that in a recent study for PFP on Ag(111), the same reflection was observed;<sup>45</sup> however, the structure was not solved by grazing-incidence X-ray diffraction. This finding is corroborated by supporting confocal Raman microscopy, which points toward the presence of a PFP phase significantly different to the single-crystal polymorph (see Supporting Information). To determine its unit cell parameters, we performed grazing-incidence X-ray diffraction (GIXRD); the corresponding reciprocal space map (RSM) is depicted in Figure 1c (top). The map can be indexed with the triclinic unit cell parameters of  $a = 15.13 \text{ \AA}$ ,  $b = 8.94 \text{ \AA}$ ,  $c = 6.51 \text{ \AA}$ ,  $\alpha = 78.56^\circ$ ,  $\beta = 108.14^\circ$ , and  $\gamma = 92.44^\circ$ , yielding a cell volume of 820  $\text{\AA}^3$ , which is essentially identical to that of the (monoclinic) TFP (816  $\text{\AA}^3$ ). This similarly suggests the presence of two molecules per unit cell ( $Z = 2$ ) also for the PSP; for the PFP/HOPG reference, identical growth was found via GIXRD-RSM (see Supporting Information). Coming back to Figure 1b, the unit cell parameters allow assignment of the specular peak to the PSP(002) reflection.

While the peak positions in GIXRD investigations (Figure 1c) allow precise determination of the unit cell dimensions, the peak intensities provide information on the molecular orientation within the unit cell. One has to bear in mind, however, that taking the experimental intensities from GIXRD as a measure for the structure factors of the PSP requires a perfectly fiber-textured film. This makes the straightforward approach

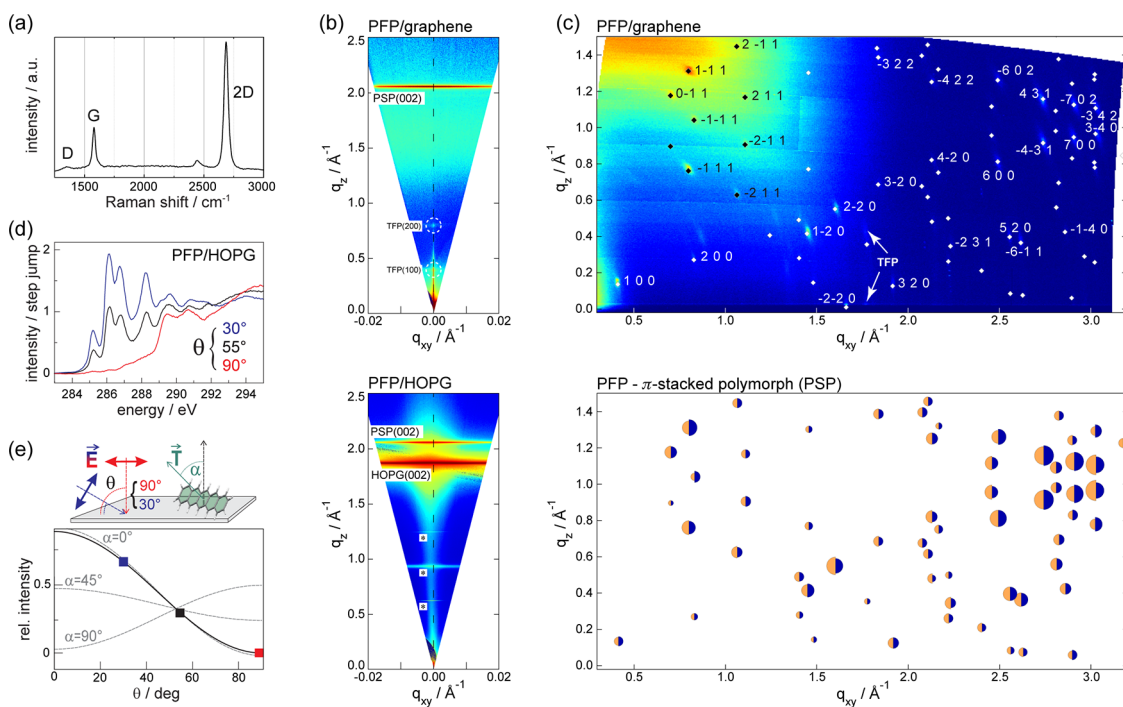


**Figure 1.** (a) Representative Raman spectrum of the graphene/quartz substrate. (b) Specular XRD scans of PFP/graphene (top) and PFP/HOPG as reference (bottom) both showing the PSP(002) reflection. For PFP/HOPG, the HOPG(002) reflection dominates the spectrum (higher harmonics of the substrate marked by stars), while no such diffraction is observed for PFP/graphene; there, minor contributions of standing PFP grown in the TFP, likely related to nucleation on substrate defects,<sup>40</sup> are found. (c) Top: GIXRD-RSM of PFP/graphene yielding the PSP unit cell dimensions. Bottom: Results of the full structure solution of the PSP; blue and orange half-circle areas compare the calculated to experimental structure factors deduced from the RSM of the PFP/HOPG reference (Supporting Information); values normalized to the (600) peak. (d) Supporting NEXAFS spectra of PFP/HOPG recorded at different incidence angles  $\theta$  of the beam indicate a strong dichroism of PFP; spectra were corrected by a subtraction of weighted HOPG substrate contributions. (e) Quantitative evaluation of the dichroism indicates an essentially lying molecular conformation;  $\vec{E}$  denotes the electric field vector of the beam, and  $\alpha$  the angle between the transition dipole moment  $\vec{T}$  and the sample normal.

of fitting the molecular orientation against the experimental intensities<sup>24</sup> problematic on graphene, where neighboring grains might exhibit a nonrandom angular relation. Recently, we presented a method to model the molecular orientation of a similar rod-like OSC by force-field calculations, where the only experimental input was the unit cell dimensions deduced from GIXRD.<sup>46</sup> Following the same approach for rigid PFP molecules confined in the PSP unit cell, we derive a full structure solution for the PSP, which is characterized by almost parallel molecular axes and planes (deviations below 4°), as illustrated in Figure 2b. To further validate this surprising result, we followed three independent approaches: (i) We employed crystal structure prediction methods<sup>47</sup> constrained to the experimental PSP unit cell with an ensuing comparison to the experimental peak intensities determined for the PFP/HOPG reference, which is fiber-textured; subsequently lifting the constraints corroborates the PSP being a local minimum crystal structure. (ii) We carried out a direct fit of the molecular orientation against the experimental intensities using the software package FOX,<sup>48</sup> which became feasible owing to the large number of reflections in the corresponding map on the (fiber-textured) PFP/HOPG reference. Both approaches led to essentially

identical results and fully confirm our structure solution (see Supporting Information for further details). Note that our structure solution fully covers the absence of the PSP(001) reflection in Figure 1b despite the triclinic crystal class of the PSP, where no systematic extinctions occur. The calculated intensity ratio of the PSP(001) to the PSP(002) reflection is 1:10 000, which cannot be experimentally observed. Furthermore, the high intensity of the (113−1) in-plane reflection (Figure 3b) corresponding to planes perpendicular to the long molecular axis is covered by our solution. (iii) Entirely independent from X-ray diffraction, we performed near-edge X-ray absorption fine structure spectroscopy (NEXAFS). Because identical growth on both graphene and HOPG is evidenced by XRD, we carried out NEXAFS on the PFP/HOPG reference to avoid known issues of NEXAFS on (large-area) epitaxial, azimuthally anisotropic organic films,<sup>49,50</sup> hence exploiting the fiber texture of the HOPG substrate (Supporting Information). The spectra in Figure 1d show a strong dichroism indicating a preferential molecular orientation in the film. Because the lower-energy peaks correspond to excitations of C1s electrons into unoccupied  $\pi^*$  orbitals ( $\pi^*$  resonances) and the corresponding transition dipole moments in PFP (denoted as  $T$  in Figure 1e) are

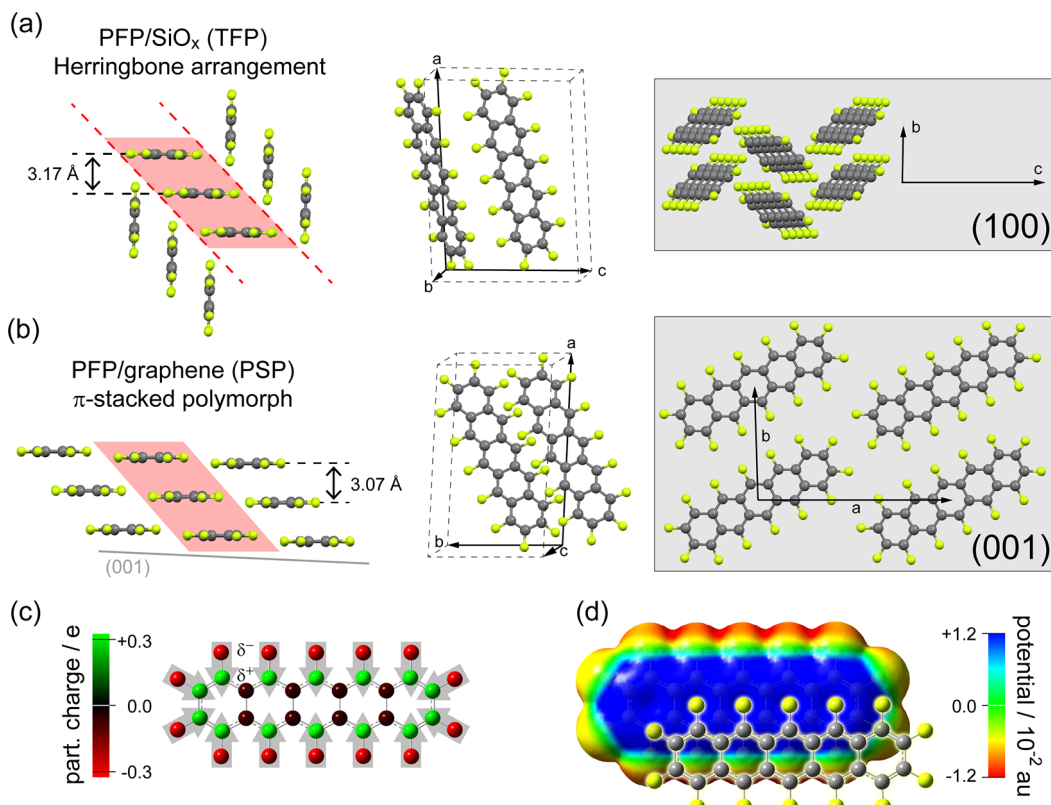


**Figure 2.** Comparison of the molecular arrangement in the two polymorphs of PFP determined in this work. (a) Herringbone arrangement of the TFP on  $\text{SiO}_x$  viewed along the long molecular axes (left), illustrated within the unit cell (middle), and as a top view on the (100) texture plane<sup>37,38</sup> (i.e., along the  $a^*$  axis) (right). (b)  $\pi$ -Stacked arrangement of the PSP viewed along the long molecular axes (left), within the unit cell (middle), and as a top view on the (001) texture plane parallel to graphene (i.e., along the  $c^*$  axis) (right). Similar  $\pi$ -stacked motifs are shaded in red;  $\pi$ -stacking distances are indicated. (c) Calculated atomic charges on the constituting atoms of a PFP molecule. (d) Calculated molecular electrostatic potential map (in atomic units) of an individual PFP molecule with an adjacent molecule within the parallel-displaced stacked motif of the PSP.

oriented perpendicular to the molecular plane,<sup>51</sup> their gradual intensity change from grazing ( $30^\circ$ ) to normal incidence of the primary beam confirms essentially *flat-lying molecules* in the PSP. This is clearly seen by a comparison of the experimental angle dependence of the  $\pi^*$  resonance intensity to calculated values, as shown in Figure 1e.

Although exceedingly different from both the TFP and the single-crystal polymorph, where a HB arrangement with a HB angle of almost  $90^\circ$  is found (Figure 2a), the severe change in molecular arrangement appears counterintuitive only at first glance. Noncovalently bound molecular assemblies, be it of HB or  $\pi$ -stacked type, result from a competition of electrostatic and dispersion interactions. It is understood that a parallel-displaced stacking motif of  $\pi$ -conjugated molecules is due to an interplay between a favorable dispersion component through the  $\pi$ -electron system (frequently termed  $\pi-\pi$  interaction) and unfavorable electrostatic effects, which are minimized by lateral displacement.<sup>52</sup> PFP exhibits strong intramolecular polar bonds (IPBs) between the highly electronegative fluorine atoms carrying a negative partial charge  $\text{F}[\delta^-]$  and the backbone carbon atoms  $\text{C}[\delta^+]$ , which translates into local

dipole moments pointing symmetrically toward the molecular core,<sup>53–55</sup> as sketched in Figure 2c. In addition to dispersion forces, such local dipoles/multipoles impact the intermolecular arrangement,<sup>56–59</sup> and in the present case, attractive dipole–dipole interactions between adjacent PFP molecules further stabilize the parallel-displaced arrangement of PFP, as illustrated by the electrostatic potential map in Figure 2d. Note that this is in stark contrast to (nonfluorinated) PEN, where such strong IPBs do not exist and HB arrangement is found in *all* polymorphs with mutually inclined molecular planes; for GIXRD of PEN/HOPG and a discussion of growth (dis-)similarities between PFP and PEN, see the Supporting Information. A closer inspection of the PFP polymorphs reveals that a similarly stacked motif is, in fact, present in both the HB and the  $\pi$ -stacked arrangement, as highlighted in red in Figure 2a,b. On graphene, the molecules are laterally shifted such that four fluorine atoms of one molecule lie exactly in the ring center of the other while being translated by one ring along the long molecular axis, which optimizes the mutual orientation of the local dipole moments associated with the IPBs (Figure 2d). The remaining major difference between the two

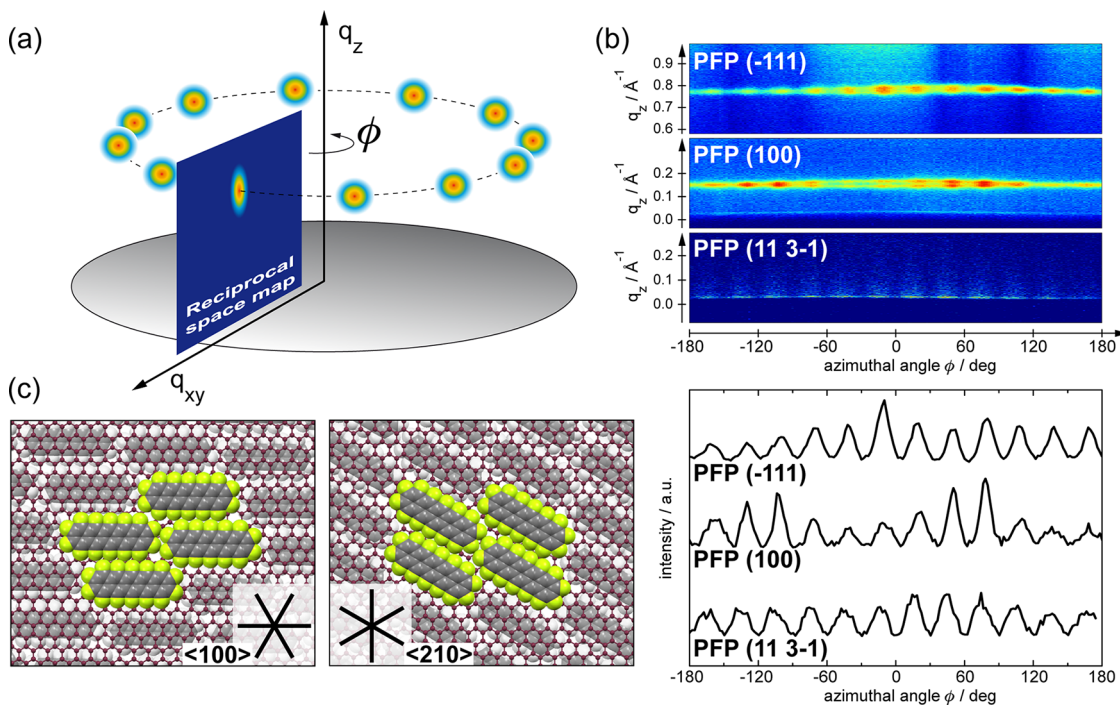


**Figure 3.** (a) Cartoon of the principle of GIXRD texture analysis. For epitaxially ordered films, discrete peaks are observed, which degenerate to circles for fiber-textured films. (b) Scans around the azimuthal angle  $\phi$  for the three strong reflections ( $-111$ ),  $(100)$ , and  $(11\ 3-1)$  of the PSP, each showing 12 maxima (top). Integration of the data along the out-of plane component of the scattering vector ( $q_z$ ) yields line scans (bottom);  $\phi$  axes were transformed from the experimental  $2+2$  geometry<sup>66</sup> to common pole figure geometry (Supporting Information). (c) Cartoon of the two suggested alignments of PFP in multilayer films (top view on the PSP(001) plane) with the graphene lattice along its two high-symmetry directions  $\langle 100 \rangle$  and  $\langle 210 \rangle$ . As these directions are crystallographically and energetically highly different but the observed intensities (b) do not alternate, an alignment with  $\langle 210 \rangle$  appears improbable (see text).

polymorphs is merely the  $\sim 90^\circ$  HB angle in the TFP, which can, in principle, be thought of as being constructed by mirroring the stack at the dotted lines in Figure 2. Importantly, the  $\pi$ -stacking distance is significantly reduced from the HB structures (single-crystal phase,  $3.26\ \text{\AA}$ ; TFP,  $3.17\ \text{\AA}$ ) to  $3.07\ \text{\AA}$  in the  $\pi$ -stacked PSP on graphene, which is among the lowest  $\pi$ -stacking distances ever reported for organic semiconductor crystal lattices.<sup>23</sup>

Clearly, since identical preparation parameters on  $\text{SiO}_x$  and graphene lead to the growth of stable films in two highly different crystal structures, the nature of the substrate emerges as the decisive factor for the selection of the respective polymorph during growth.<sup>60,61</sup> Recently, the surface unit cell of the closely packed PFP monolayer on HOPG<sup>62</sup> and on metallic substrates was determined by both scanning tunneling microscopy<sup>63–65</sup> and electron diffraction<sup>51</sup> to be almost identical to that found here for the molecules on the (001) texture plane of the PSP ( $17.2\ \text{\AA} \times 8.9\ \text{\AA}$ ,  $\angle 61^\circ$ ), as illustrated in Figure 2b. In analogy to metals and HOPG, the formation of a flat-lying PFP monolayer is expected for the graphene substrate and subsequent multilayer growth is kinetically stabilized by the monolayer arrangement<sup>60</sup> in the almost identical 3D packing motif of the PSP. As the PSP crystal structure results also from our crystal structure prediction approach, where the substrate is

not taken into account (*vide supra*), the PSP is indeed a local energetic minimum that is selected by the substrate. Note that in a previous study<sup>40</sup> the PSP was observed also in significantly thicker films on HOPG without any evidence of a thickness-driven phase transition to HB. This finding demonstrates the importance of control over the initial OSC growth to achieve desired structural properties in functional films.

Graphene as a substrate not only induces growth in the  $\pi$ -stacked polymorph but also further leads to three-dimensional *epitaxial* growth of uniaxially aligned, flat-lying PFP molecules. This is best envisioned employing GIXRD texture analysis<sup>67</sup> *via* sample rotation around the texture axis (sample normal) by  $\phi = 360^\circ$ , as illustrated in Figure 3a. There, modulations in peak intensity for given net planes appear in  $\phi$  scans if the crystallites exhibit a preferential azimuthal orientation around the texture axis instead of a perfect fiber texture ("2D powder") that would occur as homogeneous intensity distribution instead. Clearly, for PFP/graphene, we find a strong intensity modulation with 12 equidistant maxima for three selected strong PFP reflections [ $(-111)$ ,  $(100)$ , and the strong in-plane reflection  $(11\ 3-1)$ ], which exhibit an angular relation in  $\phi$  that perfectly agrees with the PSP unit cell determined above (Figure 3b). Given the active spot size of the X-ray beam in the range of  $1\ \text{mm}^2$ , this result

implies epitaxial order of the adsorbate in 12 preferential rotational domains at this length scale, which is possible due to the correspondingly large grain size of the copper foil upon thermal annealing (close to the melting temperature of Cu) during CVD graphene, which is reported to be beyond several millimeters.<sup>43,68</sup> Importantly, the finding of 12 reflections instead of 6, as it would be expected from the 6-fold symmetry of the graphene lattice, can have two causes, which, however, cannot be directly discriminated by the present area averaging experiments. First, the CVD-grown graphene substrate itself exhibits 12-fold symmetry caused by its growth on the copper foil, which is predominantly (100)-textured due to thermal treatment prior to graphene formation.<sup>68</sup> Therefore, there are two equivalent ways for the (6-fold symmetric) graphene layer to align with a supporting (4-fold symmetric) copper grain, finally leading to the observed 12-fold symmetry of the graphene layer.<sup>43,44</sup> The epitaxially grown PFP film aligns to graphene in a single-well-defined manner, thus adopting the substrate's foldness. Second, there exist two high-symmetry directions for the 6-fold symmetric graphene itself, the ⟨100⟩ ("zigzag") and the ⟨210⟩ ("armchair") directions.<sup>69</sup> The long molecular axis of PFP might align with either (Figure 3c), yielding a total of 24 orientations, of which only 12 are distinct. However, given that these two directions of graphene must be expected to be both crystallographically and energetically different, while no azimuthal alternation in intensity of the diffraction peaks (Figure 3b) is observed, we prefer explanation one. Note that growth in the (00–1) mirror texture cannot explain the observed 12 reflections, as upon molecular alignment with the high-symmetry directions the reflections of both textures coincide (Supporting Information). We stress that epitaxial growth on graphene observed here for PFP is by far not self-evident, as, for example, the related organic semiconductor perylene-3,4,9,10-tetracarboxylic acid dianhydride (PTCDA) does not epitaxially arrange with graphene.<sup>70</sup>

Having established the crystal structure of  $\pi$ -stacked PFP, we finally turn to investigating its impact on the electronic properties, that is, in particular, the transfer integral  $t$  crucial for charge transport, as outlined above. To that end, we carried out ultraviolet photo-electron spectroscopy (UPS) on the PSP under variation of the energies ( $h\nu$ ) of the incident photons at normal emission (Figure 4) to observe intermolecular energy-band dispersion along the surface normal. To avoid sample-charging issues due to the insulating quartz substrates coated by graphene, we performed UPS on PFP/HOPG, where growth in the PSP was likewise found by XRD (*vide supra*). For UPS experiments, a lower nominal film thickness of 10 nm was chosen, which is, on the one hand, sufficiently low to avoid sample charging issues and, on the other hand, large enough to avoid an influence of the HOPG substrate on the PFP electronic

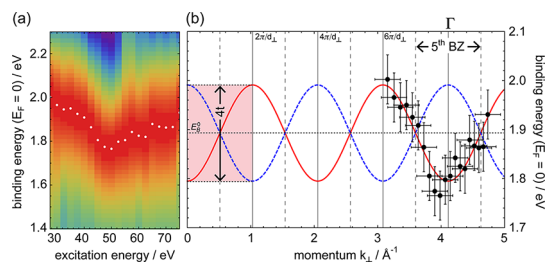


**Figure 4.** Electron band dispersion of the  $\pi$ -stacked PFP polymorph along the sample normal. (a) Second derivative of the UPS spectra for different excitation energies in the range of the HOMO emission; data represented as photo-emission intensity map with fitted peak maxima indicated as white dots (intensity normalized to the respective maxima); binding energy ( $E_b$ ) given with respect to the Fermi level ( $E_F$ ). (b) Experimental dispersion of the HOMO band depicted in the extended zone scheme with parameters of  $d_{\perp} = 6.11 \text{ \AA}$ ,  $E_b^0 = 1.89 \text{ eV}$ ,  $t = 0.05 \text{ eV}$ , and  $V_0 = -11.7 \text{ eV}$ , which compare well to literature values of related systems.<sup>39</sup> The dispersion is illustrated by two tight-binding cosine functions (red and blue curves with  $d_{\perp}/2$ ) as the PSP unit cell contains two molecules; the derived value of  $d_{\perp}$  equals the (001) lattice spacing of the PSP.

structure. From the UPS data, a value of the ionization energy of 6.0 eV is determined, which is in line with lying PFP<sup>71</sup> (see Supporting Information for raw data). According to the tight-binding model (assuming a parabolic free-electron-like band as the final continuum state), the energy-band dispersion relation is given by<sup>39,72</sup>  $E_b(k_{\perp}) = E_b^0 - 2t \cos(k_{\perp}d_{\perp})$  with  $k_{\perp} = (2m_e^*/\hbar^2)^{1/2}(E_{kin} - V_0)^{1/2}$ , where  $E_{kin} = h\nu - E_b$  is the kinetic energy of the photoelectron,  $E_b$  its binding energy from the vacuum level,  $k_{\perp}$  its wave vector component along the surface normal,  $E_b^0$  the energy of the band center,  $t$  the transfer integral,  $d_{\perp}$  the lattice spacing normal to the surface (here, the (001) spacing of the PSP),  $m_e^*$  the effective mass of the photoelectron in the final continuum state (approximated by the free electron mass  $m_0$ ), and  $V_0$  the inner potential. For experimentally assessing  $t$ , we varied  $h\nu$  from 27.5 to 75 eV (at room temperature) and determined the maxima of the HOMO band by forming the second derivative of the UPS data for each  $h\nu$ , as depicted in Figure 4a. The HOMO emission maxima shift toward lower binding energy with a minimum around  $h\nu = 50 \text{ eV}$ , where the shift is reversed. These data translate into a dispersion relation  $E_b(k_{\perp})$ , as illustrated in Figure 4b in the extended zone scheme, where the investigated  $h\nu$  range corresponds to excitation in the 4th–6th Brillouin zones. For the experimentally observed (001) lattice spacing, the data can be fitted with a cosine function according to the tight-binding model, which yields a value of 0.05 eV for the transfer integral  $t$  of the PSP; this value equals that for likewise vertically  $\pi$ -stacked PTCDA analogously determined on HOPG as substrate<sup>73</sup> and is even larger than that recently found for picene single crystals.<sup>74</sup> Finally, in a broad-band model ( $W > k_B T$ ), this allows estimating the hole mobility at room temperature for the PSP in the vertical direction to  $\mu_h > 20(m_0/m_h^*) \approx 9.6 \text{ cm}^2/(\text{V}\cdot\text{s})$ , with

the (tight-binding approximated) effective hole mass of  $m_h^* = \hbar^2/(2td_{\perp}^2) \approx 2.08 m_0$ <sup>39,75</sup>

## CONCLUSIONS

We demonstrated that coating transparent quartz substrates with graphene induces lying and coplanar  $\pi$ -stacked growth in thin PFP films. We determined the unit cell parameters of this substrate-mediated PFP polymorph by GIXRD and carried out a full structure solution both by theoretical structure modeling and fitting experimental data. Compared to the herringbone-type polymorphs of PFP, our structure solution reveals a significantly reduced  $\pi$ -stacking distance of 3.07 Å for PFP on graphene, which is among the lowest values

reported so far for organic semiconductors, giving rise to distinct electronic band dispersion along the  $\pi$ -stacking direction, as observed by UPS. Finally, we showed that substrate coating with graphene induces large-scale epitaxial growth of the vertically  $\pi$ -stacked molecules, which is expected to maximize the vertical  $\pi$ -orbital overlap being beneficial for the out-of-plane charge-carrier mobility. Our study underlines the versatility of graphene and its high potential as coating for establishing transparent electrodes in future optoelectronic applications, where vertical charge transport is generally disfavored by an edge-on standing molecular orientation on ITO-coated glass as a typical substrate.

## METHODS

**Materials and Sample Preparation.** Perfluoropentacene (PFP) (Kanto Denka Kogyo Co., 99% purity) was deposited *via* evaporation from resistively heated quartz crucibles (deposition rate = 0.5 nm/min monitored with a quartz crystal microbalance, base pressure  $<5 \times 10^{-8}$  mbar). Graphene-coated quartz pieces ( $2 \times 2 \text{ cm}^2$ ) served as substrates that were established in analogy to the procedure reported in refs 41 and 42 using a Cu foil ( $7 \times 7 \text{ cm}^2$ , 25 μm thickness, 99.8% purity, Alfa Aesar, product no. 13382, annealed for 40 min at 1020 °C) for CVD graphene growth with an ensuing wet transfer to the quartz support. Highly oriented pyrolytic graphite (ZYA-grade,  $1 \times 1 \text{ cm}^2$ ) that was *ex situ* cleaved was used as the reference substrate.

**Characterizations.** Specular and grazing-incidence X-ray diffraction (GIXRD) were performed *ex situ* at beamline W1.1 of the synchrotron radiation source HASYLAB (DESY, Germany;  $h\nu = 10.5$  keV, inert He atmosphere) with an incident beam angle of 0.15° using a MYTHEN 1D detector. Data processing was carried out using the self-implemented software package PyGid,<sup>76</sup> including intensity corrections according to ref 66 and a correction of refraction effects.

NEXAFS was performed at the HE-SGM dipole beamline of the synchrotron storage ring BESSY II in Berlin (Germany) providing linear polarized light (polarization factor = 0.91; energy resolution at the carbon K-edge = 300 meV). All NEXAFS spectra were recorded in partial electron-yield mode using a channel-plate detector with a retarding field of –150 V. For the calibration of the absolute energy scale, the photocurrent from a carbon-coated gold grid in the incident beam (absorption maximum = 284.9 eV) was recorded simultaneously. To determine the average tilt angle of the molecules relative to the sample surface, measurements were carried out at three different angles of incidence (30, 55, and 90°); for further details, see the Supporting Information.

Ultraviolet photoelectron spectroscopy (UPS) experiments were performed under ultrahigh vacuum conditions at the endstation SurICat at the synchrotron light source BESSY II (Helmholtz Zentrum Berlin für Materialien und Energie, Germany) with an energy resolution of 120 meV using excitation photon energies of 27.5–75 eV; the secondary electron cutoff was recorded at –10 V sample bias.

**Force-Field Calculations.** To determine the molecular orientation within the experimentally determined unit cell of the  $\pi$ -stacked polymorph, we utilize a global total energy minimization scheme employing force fields as described in detail in ref 46. To summarize our approach, we consider the PFP molecules as rigid bodies and search for the molecular orientations, which minimize the total energy. We consider the three spatial coordinates of the molecular center of mass as well as the three Euler angles representing the molecular orientation with respect to the unit cell frame as degrees of freedom. Thus, in total, there are  $6Z$

degrees of freedom, where  $Z$  is the number of molecules in the unit cell. To calculate the total energy of the PFP crystal, we use empirical interatomic force fields, in particular, the MM3 force field<sup>77–79</sup> as implemented in the TINKER code,<sup>80</sup> and further checked the influence of the particular choice of force field on the structure solution. To this end, we also utilized the DREIDING force field<sup>81</sup> as implemented in the GULP code,<sup>82</sup> which led to the same structure solutions as already found with MM3. For the global minimum search, we utilize a genetic algorithm (GA) for exploring the configuration space. Details on our implementation of the GA are given in the Appendix of ref 46. In order to ensure that the best crystal structure solution is indeed found, the GA optimization run has been repeated a sufficient amount of times.

Comparing the total energies of the crystal structure solutions, that is, the herringbone (HB)-type thin-film polymorph (TFP) observed on  $\text{SiO}_x$  and the  $\pi$ -stacked polymorph (PSP) on graphene (and HOPG), the energy per molecule in the PSP is found to be  $\approx 24$  meV *higher* than that in the TFP. In fact, this result confirms the observation that, apart from the PSP observed here on graphene coatings, all known PFP polymorphs tend to form a HB arrangement. Otherwise, the strong interaction of the molecules with graphene (or HOPG), which is considered only indirectly in our simulation by using the experimental crystal structure, is responsible for stabilizing the  $\pi$ -stacked packing in the molecular assemblies.

**Crystal Structure Prediction.** Possible crystal structures are predicted by systematically searching the potential energy hypersurface to identify its local minima. These minima represent the possible configurations of mechanical equilibrium and thus constitute the “natural” or “inherent” structures that the crystalline system can exhibit.<sup>83</sup> About 20 000 initial configurations were generated for PFP films on graphene, evenly distributed among the various possible arrangements consistent with the known structural information, that is, a triclinic unit cell (with the experimental lattice parameters reported in this article) containing two molecules ( $Z = 2$ ). The triclinic lattice allows only two space groups:  $P\bar{1}$  (no symmetry) and  $P\bar{1}$  (inversion symmetry only). In  $P\bar{1}$ , the molecules have inversion symmetry and are therefore allowed (but not required) to lie on one of the eight possible inversion sites (with coordinates  $x,y,z$  equal to 0 or 1/2). The various possibilities thus are  $P\bar{1}$  with  $Z = 2$  (1) (a molecule on a generic site “1”, plus a second equivalent molecule obtained by inversion),  $P\bar{1}$  with  $Z = 2$  ( $\bar{1},\bar{1}$ ) (two independent molecules on inversion sites “1”), or  $P\bar{1}$  with  $Z = 2$  (1,1) (two independent molecules, one chosen as the origin, the other at generic coordinates).

Starting from each initial configuration, we minimize the potential energy. The molecules are treated as rigid units with the  $D_{2h}$  planar geometry determined with Gaussian 03,<sup>84</sup> using the B3LYP/6-31G\* combination of density functional and basis set. They interact through a pairwise additive atom–atom

**TABLE 1. Experimental<sup>36,37</sup> and Computed Lattice Parameters (axes in Å, angles in degrees)**

lattice	structure	<i>a</i>	<i>b</i>	<i>c</i>	$\alpha$	$\beta$	$\gamma$
$P_2/c$ $Z = 2$ ( $\bar{1}\bar{1}$ )	single-crystal PFP <sup>36</sup>	expt	15.51	4.49	11.45	90.00	91.57
							90.00
	PFP on $\text{SiO}_x$ (TFP) <sup>37</sup>	expt	15.76	4.51	11.48	90.00	90.40
							90.00
$\bar{P}1$ $Z = 2$ ( $\bar{1},\bar{1}$ )	PFP on graphene (PSP)	expt	15.13	8.94	6.51	78.56	108.14
							92.44
		calcd	15.69	4.53	12.03	90.00	90.15
							90.00
		calcd	15.20	9.00	6.87	75.92	108.33
							92.16

potential model of the form  $V(r) = A_{ij}/r^{12} - B_{ij}/r^6 + q_i q_j/r$ , which combines a Lennard-Jones potential model with the DREIDING<sup>81</sup> parameters ( $A_{ij}$  and  $B_{ij}$ ) with a Coulombic contribution described by atomic charges  $q_i$ . These parameters are fitted to the electrostatic potential in the isolated molecule.<sup>84</sup> Structural optimization initially proceeded with lattice parameters fixed to the experimental values. Once found all distinct constrained minima [see the Supporting Information (S1) for one in perfect agreement with the experimental intensities], we then continued the energy minimization without constraints, by adjusting also the unit cell axes and angles. We suppose that surface-induced polymorphs, although not necessarily coincident with genuine local minima of the potential energy, cannot be too unstable. Structures which move too far (once removed the constraints on the lattice parameters) or that fail to converge to stable bound states (*i.e.*, to high-density structures with negative potential energy) are unlikely to be correct and are therefore discarded. Bulk crystal structures were also searched, using the methods extensively discussed in previous work<sup>85,86</sup> to obtain information on the global stability of the minima and to validate the potential model. We have, thus, generated and optimized (without constraints) several thousands of additional monoclinic structures in the space group  $P_2/c$  with  $Z = 2$  (the structure of both the TFP and the single-crystal phase). The potential model appears quite realistic since these two known structures (single-crystal phase<sup>36</sup> and TFP on  $\text{SiO}_x$ <sup>37</sup>) both converge to very deep minima (rank 2) and are reproduced extremely well by the calculations (see Table 1).

We suppose that surface-induced forms should closely resemble local minima of the potential energy (inherent structures). The idea is that the interactions with the surface will mostly increase the energetic and/or kinetic stability of minima that already exist, rather than creating brand new minima. This idea is almost certainly correct for weakly interacting surfaces such as  $\text{SiO}_x$ , where the known structure (TFP)<sup>37</sup> is closely related to the single-crystal structure.<sup>36</sup> The idea is probably also correct also for PFP on graphene, where a flat-lying monolayer is expected and subsequent multilayer growth is kinetically stabilized by the monolayer arrangement in the almost identical 3D packing motif of the  $\pi$ -stacked polymorph determined in this work (with significant initial theoretical input but fully confirmed by the X-ray diffraction experiments). In fact, it converges to a very deep minimum (rank 3), and again, the computed lattice parameters are in good agreement with the experiments (see Table 1).

**Calculation of Atomic Charges.** Density functional theory (DFT) calculations of the atomic charges on the atoms forming a PFP molecule and of the molecular electrostatic potential map (Figure 2c,d) relied on the hybrid exchange-correlation functional PBE0<sup>87</sup> and a 6-31G\*\* contracted Gaussian basis set.<sup>88,89</sup> Atomic charges reported in Figure 2 were obtained through a Mulliken analysis;<sup>90</sup> calculations were performed with the Gaussian 09 quantum chemistry suite.<sup>91</sup>

**Conflict of Interest:** The authors declare no competing financial interest. \*Present address: Humboldt-Universität zu Berlin, Institut für Physik, Berlin, Germany. ^Present address: Karl-Franzens-Universität Graz, Institut für Physik, Graz, Austria.

**Acknowledgment.** We thank Wolfgang Caliebe (DESY-HASYLAB) for experimental support and granting access to the very last photons from storage ring DORIS before its final shutdown on October 22, 2012 [for the last spectrum (PFP/quartz) recorded at beamline W1.1, see the Supporting Information]. We further acknowledge Ruslan Ovsyannikov [Helmholtz-Zentrum Berlin (HZB), BESSY II] for experimental support, Roland Resel (TU Graz, Austria) for support in unit cell determination, and the HZB for granting access to beamline HE-SGM and to the optics beamline (SurfCat), as well as the HZB and DESY for travel support. T.B. gratefully acknowledges the Friedrich-Ebert-Stiftung (Germany) for financial support. Financing through the DFG (Germany) and the Austrian Science Fund (FWF): [P21094] and [S9714] is gratefully acknowledged.

**Supporting Information Available:** Crystallographic information files (CIFs), structure solution of the PFP/ $\text{SiO}_x$  thin-film phase (TFP), UPS data, GIXRD on PFP/HOPG, XRD comparison between PFP on graphene-coated and pristine quartz, XRD rocking curve of PFP/graphene, quantitative NEXAFS analysis, and Raman spectroscopy of PFP/HOPG; methodological remarks on XRD geometries, GIXRD texture analysis in 2 + 2 geometry, relation between the PSP (001) and (00-1) textures; a comparison of the results of the three independent approaches to structure solution. This material is available free of charge via the Internet at <http://pubs.acs.org>.

## REFERENCES AND NOTES

- Geim, A. K. Graphene: Status and Prospects. *Science* **2009**, *324*, 1530–1534.
- Geim, A. K.; Novoselov, K. S. The Rise of Graphene. *Nat. Mater.* **2007**, *6*, 183–191.
- Lee, C.; Wei, X. D.; Kysar, J. W.; Hone, J. Measurement of the Elastic Properties and Intrinsic Strength of Monolayer Graphene. *Science* **2008**, *321*, 385–388.
- Castro Neto, A. H.; Guinea, F.; Peres, N. M. R.; Novoselov, K. S.; Geim, A. K. The Electronic Properties of Graphene. *Rev. Mod. Phys.* **2009**, *81*, 109–162.
- Lin, Y. M.; Dimitrakopoulos, C.; Jenkins, K. A.; Farmer, D. B.; Chiu, H. Y.; Grill, A.; Avouris, P. 100-GHz Transistors from Wafer-Scale Epitaxial Graphene. *Science* **2010**, *327*, 662–662.
- Schedin, F.; Geim, A. K.; Morozov, S. V.; Hill, E. W.; Blake, P.; Katsnelson, M. I.; Novoselov, K. S. Detection of Individual Gas Molecules Adsorbed on Graphene. *Nat. Mater.* **2007**, *6*, 652–655.
- Liu, M.; Yin, X. B.; Ulin-Avila, E.; Geng, B. S.; Zentgraf, T.; Ju, L.; Wang, F.; Zhang, X. A Graphene-Based Broadband Optical Modulator. *Nature* **2011**, *474*, 64–67.
- Pang, S. P.; Hernandez, Y.; Feng, X. L.; Müllen, K. Graphene as Transparent Electrode Material for Organic Electronics. *Adv. Mater.* **2011**, *23*, 2779–2795.
- Wan, X. J.; Long, G. K.; Huang, L.; Chen, Y. S. Graphene—A Promising Material for Organic Photovoltaic Cells. *Adv. Mater.* **2011**, *23*, 5342–5358.
- Nair, R. R.; Blake, P.; Grigorenko, A. N.; Novoselov, K. S.; Booth, T. J.; Stauber, T.; Peres, N. M. R.; Geim, A. K. Fine Structure Constant Defines Visual Transparency of Graphene. *Science* **2008**, *320*, 1308–1308.
- Chen, J. H.; Jang, C.; Xiao, S. D.; Ishigami, M.; Fuhrer, M. S. Intrinsic and Extrinsic Performance Limits of Graphene Devices on  $\text{SiO}_2$ . *Nat. Nanotechnol.* **2008**, *3*, 206–209.
- Bae, S.; Kim, H.; Lee, Y.; Xu, X. F.; Park, J. S.; Zheng, Y.; Balakrishnan, J.; Lei, T.; Kim, H. R.; Song, Y. I.; et al. Roll-to-Roll Production of 30-Inch Graphene Films for Transparent Electrodes. *Nat. Nanotechnol.* **2010**, *5*, 574–578.
- Kim, K. S.; Zhao, Y.; Jang, H.; Lee, S. Y.; Kim, J. M.; Kim, K. S.; Ahn, J. H.; Kim, P.; Choi, J. Y.; Hong, B. H. Large-Scale Pattern Growth of Graphene Films for Stretchable Transparent Electrodes. *Nature* **2009**, *457*, 706–710.
- Brédas, J. L.; Calbert, J. P.; da Silva Filho, D. A.; Cornil, J. Organic Semiconductors: A Theoretical Characterization of the Basic Parameters Governing Charge Transport. *Proc. Natl. Acad. Sci. U.S.A.* **2002**, *99*, 5804–5809.

15. Copceanu, V.; Cornil, J.; da Silva Filho, D. A.; Olivier, Y.; Silbey, R.; Brédas, J. L. Charge Transport in Organic Semiconductors. *Chem. Rev.* **2007**, *107*, 926–952.
16. Kera, S.; Yamane, H.; Ueno, N. First-Principles Measurements of Charge Mobility in Organic Semiconductors: Valence Hole-Vibration Coupling in Organic Ultrathin Films. *Prog. Surf. Sci.* **2009**, *84*, 135–154.
17. Anthony, J. E. Functionalized Acenes and Heteroacenes for Organic Electronics. *Chem. Rev.* **2006**, *106*, 5028–5048.
18. Desiraju, G. R.; Gavezzotti, A. Crystal-Structures of Poly-nuclear Aromatic-Hydrocarbons—Classification, Rationalization and Prediction from Molecular-Structure. *Acta Crystallogr., B* **1989**, *45*, 473–482.
19. Lee, J. Y.; Roth, S.; Park, Y. W. Anisotropic Field Effect Mobility in Single Crystal Pentacene. *Appl. Phys. Lett.* **2006**, *88*, 252106.
20. Hoeben, F. J. M.; Jonkheijm, P.; Meijer, E. W.; Schenning, A. P. H. J. About Supramolecular Assemblies of  $\pi$ -Conjugated Systems. *Chem. Rev.* **2005**, *105*, 1491–1546.
21. Anthony, J. E.; Brooks, J. S.; Eaton, D. L.; Parkin, S. R. Functionalized Pentacene: Improved Electronic Properties from Control of Solid-State Order. *J. Am. Chem. Soc.* **2001**, *123*, 9482–9483.
22. Sheraw, C. D.; Jackson, T. N.; Eaton, D. L.; Anthony, J. E. Functionalized Pentacene Active Layer Organic Thin-Film Transistors. *Adv. Mater.* **2003**, *15*, 2009–2011.
23. Giri, G.; Verploegen, E.; Mannsfeld, S. C. B.; Atahan-Evrak, S.; Kim, D. H.; Lee, S. Y.; Becerril, H. A.; Aspuru-Guzik, A.; Toney, M. F.; Bao, Z. A. Tuning Charge Transport in Solution-Sheared Organic Semiconductors Using Lattice Strain. *Nature* **2011**, *480*, 504–509.
24. Mannsfeld, S. C.; Tang, M. L.; Bao, Z. Thin Film Structure of Trisopropylsilylithiethyl-Functionalized Pentacene and Tetraceno[2,3-b]thiophene from Grazing Incidence X-ray Diffraction. *Adv. Mater.* **2011**, *23*, 127–131.
25. Huang, H.; Chen, S.; Gao, X. Y.; Chen, W.; Wee, A. T. S. Structural and Electronic Properties of PTCDA Thin Films on Epitaxial Graphene. *ACS Nano* **2009**, *3*, 3431–3436.
26. Ren, J.; Meng, S.; Wang, Y. L.; Ma, X. C.; Xue, Q. K.; Kaxiras, E. Properties of Copper (Fluoro)-Phthalocyanine Layers Deposited on Epitaxial Graphene. *J. Chem. Phys.* **2011**, *134*, 194706.
27. Emery, J. D.; Wang, Q. H.; Zarrouati, M.; Fenter, P.; Hersam, M. C.; Bedzyk, M. J. Structural Analysis of PTCDA Monolayers on Epitaxial Graphene with Ultra-high Vacuum Scanning Tunneling Microscopy and High-Resolution X-ray Reflectivity. *Surf. Sci.* **2011**, *605*, 1685–1693.
28. Zhou, H. T.; Mao, J. H.; Li, G.; Wang, Y. L.; Feng, X. L.; Du, S. X.; Müllen, K.; Gao, H. J. Direct Imaging of Intrinsic Molecular Orbitals Using Two-Dimensional Epitaxially-Grown, Nanostructured Graphene for Study of Single Molecule and Interactions. *Appl. Phys. Lett.* **2011**, *99*, 153101.
29. Lee, W. H.; Park, J.; Sim, S. H.; Lim, S.; Kim, K. S.; Hong, B. H.; Cho, K. Surface-Directed Molecular Assembly of Pentacene on Monolayer Graphene for High-Performance Organic Transistors. *J. Am. Chem. Soc.* **2011**, *133*, 4447–4454.
30. Hlawacek, G.; Khokhar, F. S.; van Gastel, R.; Poelsema, B.; Teichert, C. Smooth Growth of Organic Semiconductor Films on Graphene for High-Efficiency Electronics. *Nano Lett.* **2011**, *11*, 333–337.
31. Scardamaglia, M.; Forte, G.; Lizzit, S.; Baraldi, A.; Lacovig, P.; Larciprete, R.; Mariani, C.; Betti, M. G. Metal-Phthalocyanine Array on the Moiré Pattern of a Graphene Sheet. *J. Nanopart. Res.* **2011**, *13*, 6013–6020.
32. Rossi, L.; Seidel, K. F.; Machado, W. S.; Hummelgen, I. A. Low Voltage Vertical Organic Field-Effect Transistor with Polyvinyl Alcohol as Gate Insulator. *J. Appl. Phys.* **2011**, *110*, 094508.
33. Ma, L. P.; Yang, Y. Unique Architecture and Concept for High-Performance Organic Transistors. *Appl. Phys. Lett.* **2004**, *85*, 5084–5086.
34. Watanabe, Y.; Kudo, K. Flexible Organic Static Induction Transistors Using Pentacene Thin Films. *Appl. Phys. Lett.* **2005**, *87*, 223505.
35. Dimitrakopoulos, C. D.; Malenfant, P. R. L. Organic Thin Film Transistors for Large Area Electronics. *Adv. Mater.* **2002**, *14*, 99–117.
36. Sakamoto, Y.; Suzuki, T.; Kobayashi, M.; Gao, Y.; Fukai, Y.; Inoue, Y.; Sato, F.; Tokito, S. Perfluoropentacene: High-Performance p-n Junctions and Complementary Circuits with Pentacene. *J. Am. Chem. Soc.* **2004**, *126*, 8138–8140.
37. Salzmann, I.; Duhm, S.; Heimel, G.; Rabe, J. P.; Koch, N.; Oehzelt, M.; Sakamoto, Y.; Suzuki, T. Structural Order in Perfluoropentacene Thin Films and Heterostructures with Pentacene. *Langmuir* **2008**, *24*, 7294–7298.
38. Kowarik, S.; Gerlach, A.; Hinderhofer, A.; Milita, S.; Borgatti, F.; Zontone, F.; Suzuki, T.; Biscarini, F.; Schreiber, F. Structure, Morphology, and Growth Dynamics of Perfluoropentacene Thin Films. *Phys. Status Solidi Rapid Res. Lett.* **2008**, *2*, 120–122.
39. Ueno, N.; Kera, S. Electron Spectroscopy of Functional Organic Thin Films: Deep Insights into Valence Electronic Structure in Relation to Charge Transport Property. *Prog. Surf. Sci.* **2008**, *83*, 490–557.
40. Breuer, T.; Salzmann, I.; Götz, J.; Oehzelt, M.; Morherr, A.; Koch, N.; Witte, G. Interrelation between Substrate Roughness and Thin-Film Structure of Functionalized Acenes on Graphite. *Cryst. Growth Des.* **2011**, *11*, 4996–5001.
41. Li, X. S.; Cai, W. W.; An, J. H.; Kim, S.; Nah, J.; Yang, D. X.; Piner, R.; Velamakanni, A.; Jung, I.; Tutuc, E.; et al. Large-Area Synthesis of High-Quality and Uniform Graphene Films on Copper Foils. *Science* **2009**, *324*, 1312–1314.
42. Ferrari, A. C.; Meyer, J. C.; Scardaci, V.; Casiraghi, C.; Lazzeri, M.; Mauri, F.; Piscanec, S.; Jiang, D.; Novoselov, K. S.; Roth, S.; et al. Raman Spectrum of Graphene and Graphene Layers. *Phys. Rev. Lett.* **2006**, *97*, 187401.
43. Huang, P. Y.; Ruiz-Vargas, C. S.; van der Zande, A. M.; Whitney, W. S.; Levendorf, M. P.; Kevek, J. W.; Garg, S.; Alden, J. S.; Hustadt, C. J.; Zhu, Y.; et al. Grains and Grain Boundaries in Single-Layer Graphene Atomic Patchwork Quilts. *Nature* **2011**, *469*, 389–393.
44. Wofford, J. M.; Nie, S.; McCarty, K. F.; Bartelt, N. C.; Dubon, O. D. Graphene Islands on Cu Foils: The Interplay between Shape, Orientation, and Defects. *Nano Lett.* **2010**, *10*, 4890–4896.
45. Duhm, S.; Hosoumi, S.; Salzmann, I.; Gerlach, A.; Oehzelt, M.; Wedl, B.; Lee, T. L.; Schreiber, F.; Koch, N.; Ueno, N.; et al. Influence of Intramolecular Polar Bonds on Interface Energetics in Perfluoro-pentacene on Ag(111). *Phys. Rev. B* **2010**, *81*, 045418.
46. Salzmann, I.; Nabok, D.; Oehzelt, M.; Duhm, S.; Moser, A.; Heimel, G.; Puschning, P.; Ambrosch-Draxl, C.; Rabe, J. P.; Koch, N. Structure Solution of the 6,13-Pentacenequinone Surface-Induced Polymorph by Combining X-ray Diffraction Reciprocal-Space Mapping and Theoretical Structure Modeling. *Cryst. Growth Des.* **2011**, *11*, 600–606.
47. Bardwell, D. A.; Adjiman, C. S.; Arnaudova, Y. A.; Bartshevich, E.; Boerrigter, S. X. M.; Braun, D. E.; Cruz-Cabeza, A. J.; Day, G. M.; Della Valle, R. G.; Desiraju, G. R.; et al. Towards Crystal Structure Prediction of Complex Organic Compounds—A Report on the Fifth Blind Test. *Acta Crystallogr., B* **2011**, *67*, 535–551.
48. Favre-Nicolin, V.; Cerny, R. FOX, 'Free Objects for Crystallography': A Modular Approach to Ab Initio Structure Determination from Powder Diffraction. *J. Appl. Crystallogr.* **2002**, *35*, 734–743.
49. Oehzelt, M.; Berkebile, S.; Koller, G.; Ivanko, J.; Surnev, S.; Ramsey, M. G.  $\alpha$ -Sexithiophene on Cu(110) and Cu(110)-(2  $\times$  1)O: An STM and NEXAFS Study. *Surf. Sci.* **2009**, *603*, 412–418.
50. Koller, G.; Berkebile, S.; Krenn, J. R.; Netzer, F. P.; Oehzelt, M.; Haber, T.; Resel, R.; Ramsey, M. G. Heteroepitaxy of Organic–Organic Nanostructures. *Nano Lett.* **2006**, *6*, 1207–1212.
51. Marks, M.; Schmidt, C.; Schwalb, C. H.; Breuer, T.; Witte, G.; Höfer, U. Temperature Dependent Structural Phase Transition at the Perfluoropentacene/Ag(111) Interface. *J. Phys. Chem. C* **2012**, *116*, 1904–1911.
52. Grimme, S. Do Special Noncovalent  $\pi$ – $\pi$  Stacking Interactions Really Exist? *Angew. Chem., Int. Ed.* **2008**, *47*, 3430–3434.
53. Tang, M. L.; Bao, Z. A. Halogenated Materials as Organic Semiconductors. *Chem. Mater.* **2011**, *23*, 446–455.

54. Heimel, G.; Salzmann, I.; Duhm, S.; Koch, N. Design of Organic Semiconductors from Molecular Electrostatics. *Chem. Mater.* **2011**, *23*, 359–377.
55. Salzmann, I.; Duhm, S.; Heimel, G.; Oehzelt, M.; Kniprath, R.; Johnson, R. L.; Rabe, J. P.; Koch, N. Tuning the Ionization Energy of Organic Semiconductor Films: The Role of Intramolecular Polar Bonds. *J. Am. Chem. Soc.* **2008**, *130*, 12870–12871.
56. Wheeler, S. E. Local Nature of Substituent Effects in Stacking Interactions. *J. Am. Chem. Soc., Perkin Trans. 2* **2001**, *133*, 10262–10274.
57. Hunter, C. A.; Lawson, K. R.; Perkins, J.; Urch, C. J. Aromatic Interactions. *J. Chem. Soc., Perkin Trans. 2* **2001**, *133*, 651–669.
58. Williams, J. H. The Molecular Electric Quadrupole-Moment and Solid-State Architecture. *Acc. Chem. Res.* **1993**, *26*, 593–598.
59. Käfer, D.; El Helou, M.; Gemel, C.; Witte, G. Packing of Planar Organic Molecules: Interplay van der Waals and Electrostatic Interaction. *Cryst. Growth Des.* **2008**, *8*, 3053–3057.
60. Djuric, T.; Ules, T.; Flesch, H. G.; Plank, H.; Shen, Q. A.; Teichert, C.; Resel, R.; Ramsey, M. G. Epitaxially Grown Films of Standing and Lying Pentacene Molecules on Cu(110) Surfaces. *Cryst. Growth Des.* **2011**, *11*, 1015–1020.
61. Djuric, T.; Ules, T.; Gusenleitner, S.; Kayunkid, N.; Plank, H.; Hlawacek, G.; Teichert, C.; Brinkmann, M.; Ramsey, M.; Resel, R. Substrate Selected Polymorphism of Epitaxially Aligned Tetraphenyl-Porphyrin Thin Films. *Phys. Chem. Chem. Phys.* **2012**, *14*, 262–272.
62. Glowatzki, H.; Heimel, G.; Vollmer, A.; Wong, S. L.; Huang, H.; Chen, W.; Wee, A. T. S.; Rabe, J. P.; Koch, N. Impact of Fluorination on Initial Growth and Stability of Pentacene on Cu(111). *J. Phys. Chem. C* **2012**, *116*, 7726–7734.
63. Wong, S. L.; Huang, H.; Huang, Y. L.; Wang, Y. Z.; Gao, X. Y.; Suzuki, T.; Chen, W.; Wee, A. T. S. Effect of Fluorination on the Molecular Packing of Perfluoropentacene and Pentacene Ultrathin Films on Ag(111). *J. Phys. Chem. C* **2010**, *114*, 9356–9361.
64. Götz, J.; Schwalb, C. H.; Schmidt, C.; Mette, G.; Marks, M.; Höfer, U.; Witte, G. Structural Evolution of Perfluoro-pentacene Films on Ag(111): Transition from 2D to 3D Growth. *Langmuir* **2011**, *27*, 993–999.
65. de Oteyza, D. G.; Wakayama, Y.; Liu, X.; Yang, W.; Cook, P. L.; Himpel, F. J.; Ortega, J. E. Effect of Fluorination on the Molecule–Substrate Interactions of Pentacene/Cu(100) Interfaces. *Chem. Phys. Lett.* **2010**, *490*, 54–57.
66. Smilgies, D. M. Geometry-Independent Intensity Correction Factors for Grazing-Incidence Diffraction. *Rev. Sci. Instrum.* **2002**, *73*, 1706–1710.
67. Oehzelt, M.; Koller, G.; Ivancic, J.; Berkebile, S.; Haber, T.; Resel, R.; Netzer, F. P.; Ramsey, M. G. Organic Heteroepitaxy: *p*-Sexiphenyl on Uniaxially Oriented  $\alpha$ -Sexithiophene. *Adv. Mater.* **2006**, *18*, 2466–2470.
68. Robinson, Z. R.; Tyagi, P.; Murray, T. M.; Ventrice, C. A.; Chen, S. S.; Munson, A.; Magnuson, C. W.; Ruoff, R. S. Substrate Grain Size and Orientation of Cu and Cu-Ni Foils Used for the Growth of Graphene Films. *J. Vac. Sci. Technol., A* **2012**, *30*, 011401.
69. Batzill, M. The Surface Science of Graphene: Metal Interfaces, CVD Synthesis, Nanoribbons, Chemical Modifications, and Defects. *Surf. Sci. Rep.* **2012**, *67*, 83–115.
70. Wang, Q. H.; Hersam, M. C. Room-Temperature Molecular-Resolution Characterization of Self-Assembled Organic Monolayers on Epitaxial Graphene. *Nat. Chem.* **2009**, *1*, 206–211.
71. Koch, N.; Vollmer, A.; Duhm, S.; Sakamoto, Y.; Suzuki, T. The Effect of Fluorination on Pentacene/Gold Interface Energistics and Charge Reorganization Energy. *Adv. Mater.* **2007**, *19*, 112–116.
72. Seki, K.; Ueno, N.; Karlsson, U. O.; Engelhardt, R.; Koch, E. E. Valence Bands of Oriented Finite Linear-Chain Molecular-Solids as Model Compounds of Polyethylene Studied by Angle-Resolved Photoemission. *Chem. Phys.* **1986**, *105*, 247–265.
73. Yamane, H.; Kera, S.; Okudaira, K. K.; Yoshimura, D.; Seki, K.; Ueno, N. Intermolecular Energy-Band Dispersion in PTCDA Multilayers. *Phys. Rev. B* **2003**, *68*, 033102.
74. Xin, Q.; Duhm, S.; Bussolotti, F.; Akaike, K.; Kubozono, Y.; Aoki, H.; Kosugi, T.; Kera, S.; Ueno, N. Accessing Surface Brillouin Zone and Band Structure of Picene Single Crystals. *Phys. Rev. Lett.* **2012**, *108*, 226401.
75. Fröhlich, H.; Sewell, G. L. Electric Conduction in Semiconductors. *Proc. Phys. Soc., London* **1959**, *74*, 643–647.
76. Moser, A.; Werzer, O.; Flesch, H. G.; Koini, M.; Smilgies, D. M.; Nabok, D.; Puschnig, P.; Ambrosch-Draxl, C.; Schiek, M.; Rubahn, H. G.; et al. Crystal Structure Determination from Two-Dimensional Powders: A Combined Experimental and Theoretical Approach. *Eur. Phys. J.* **2009**, *167*, 59–65.
77. Allinger, N. L.; Yuh, Y. H.; Lii, J. H. Molecular Mechanics: The MM3 Force-Field for Hydrocarbons 0.1. *J. Am. Chem. Soc.* **1989**, *111*, 8551–8566.
78. Lii, J. H.; Allinger, N. L. Molecular Mechanics: The MM3 Force-Field for Hydrocarbons. 2. Vibrational Frequencies and Thermodynamics. *J. Am. Chem. Soc.* **1989**, *111*, 8566–8575.
79. Lii, J. H.; Allinger, N. L. Molecular Mechanics: The MM3 Force-Field for Hydrocarbons. 3. The Vanderwaals Potentials and Crystal Data for Aliphatic and Aromatic-Hydrocarbons. *J. Am. Chem. Soc.* **1989**, *111*, 8576–8582.
80. Ponder, J. W. *TINKER: Software Tools for Molecular Design*, 5th ed.; Washington University School of Medicine: Saint Louis, MO, 2010.
81. Mayo, S. L.; Olafson, B. D.; Goddard, W. A. DREIDING: A Generic Force-Field for Molecular Simulations. *J. Phys. Chem.* **1990**, *94*, 8897–8909.
82. Gale, J. D. GULP: A Computer Program for the Symmetry-Adapted Simulation of Solids. *J. Chem. Soc., Faraday Trans. 1997*, *93*, 629–637.
83. Stillinger, F. H.; Weber, T. A. Hidden Structure in Liquids. *Phys. Rev. A* **1982**, *25*, 978–989.
84. Frisch, M. J.; Trucks, G. W.; Schlegel, H. B.; Scuseria, G. E.; Robb, M. A.; Cheeseman, J. R.; Montgomery, J. A., Jr.; Vreven, T.; Kudin, K. N.; Burant, J. C.; et al. *Gaussian 03*, revision D.02; Gaussian, Inc.: Wallingford, CT, 2004.
85. Della Valle, R. G.; Venuti, E.; Brillante, A.; Girlando, A. Inherent Structures of Crystalline Pentacene. *J. Chem. Phys.* **2003**, *118*, 807–815.
86. Della Valle, R. G.; Venuti, E.; Brillante, A.; Girlando, A. Are Crystal Polymorphs Predictable? The Case of Sexithiophene. *J. Phys. Chem. A* **2008**, *112*, 6715–6722.
87. Adamo, C.; Barone, V. Toward Reliable Density Functional Methods without Adjustable Parameters: The PBE0 Model. *J. Chem. Phys.* **1999**, *110*, 6158–6170.
88. Hehre, W. J.; Ditchfield, R.; Pople, J. A. Self-Consistent Molecular-Orbital Methods. XII. Further Extensions of Gaussian-Type Basis Sets for Use in Molecular-Orbital Studies of Organic-Molecules. *J. Chem. Phys.* **1972**, *56*, 2257–2261.
89. Hariharan, P. C.; Pople, J. A. Influence of Polarization Functions on Molecular-Orbital Hydrogenation Energies. *Theor. Chem. Acc.* **1973**, *28*, 213–222.
90. Mulliken, R. S. Electronic Population Analysis on LCAO-MO Molecular Wave Functions 1. *J. Chem. Phys.* **1955**, *23*, 1833–1840.
91. Frisch, M. J.; Trucks, G. W.; Schlegel, H. B.; Scuseria, G. E.; Robb, M. A.; Cheeseman, J. R.; Scalmani, G.; Barone, V.; Mennucci, B.; Petersson, G. A.; et al. *Gaussian 09*, revision A.02; Gaussian Inc.: Wallingford CT, 2009.